FLAME SPREAD ACROSS LIQUIDS

Howard D. Ross (NASA Lewis Research Center), Fletcher Miller (Case Western Reserve University)
David Schiller and William Sirignano (University of California, Irvine)

Introduction

Recent reviews [1,2] of our understanding of flame spread across liquids show that there are many unresolved issues regarding the phenomenology and causal mechanisms affecting ignition susceptibility, flame spread characteristics, and flame spread rates. One area of discrepancy is the effect of buoyancy in both the uniform and pulsating spread regimes. The approach we have taken to resolving the importance of buoyancy for these flames is: (a) normal gravity (1g) and microgravity (μg) experiments, and (b) numerical modeling at different gravitational levels. Of special interest to this work, as discussed at the previous workshop, is the determination of whether, and under what conditions, pulsating spread occurs in μg. Microgravity offers a unique ability to modify and control the gas-phase flow pattern by utilizing a forced air flow over the pool surface.

Normal Gravity Experiments Since Last Workshop

The subsurface temperature field was examined using rainbow schlieren deflectometry (RSD) [3], and subsurface velocity field measurements were taken using particle image velocimetry (PIV) [4] for 1g, near-flash, uniform flame spread across 1-propanol between 18 and 23 °C. Prior to ignition both the RSD and the PIV system revealed that a seemingly quiescent pool was in fact in cellular motion with velocities on the order of 2 mm/s (small compared to the flame spread rate, U_{fl}). Due to evaporative cooling, the liquid surface temperature, T_{lg}, dropped 1 °C or more compared to the bulk liquid; this change can affect U_{fl}.

One goal of this 1g work was to determine the controlling mechanism of uniform flame spread. Assuming that the 2 cm wide tray was wide enough to represent asymptotic behavior for our test conditions (uniform spread experiments in wider trays are clearly needed), the PIV revealed the onset of liquid-phase convection more than 1 cm ahead of the spreading flame; however, the flame overtook this moving surface. In flame-fixed coordinates, therefore, there was no convection away from the flame. This behavior suggests that preheating is via a mixed mode, with convection contributing along with other mechanisms, the most likely candidate being gas-phase conduction. Despite its sensitivity, the RSD system did not show any subsurface heating ahead of the flame, indicating the preheating is confined to a very thin (sub mm) surface layer. A computer program, described in [5] as well as below, was used to model the flame spread process and agreed well with the RSD observations. Both the model and the RSD results, however, are in contrast to the holographic interferometric results in [6] for reasons described in [4].

Microgravity Experiments Since Last Workshop

The experiment was flown on a Terrier-Black Brant sounding rocket; this was the first μg combustion experiment to be performed in a sounding rocket. The two major hardware components were the Experiment Package (EP) and the Avionics Package (AP). The EP housed the fuel tray test section, fuel delivery system, Data Acquisition System, and all video diagnostic systems. The AP housed the control computer, video tape recorders, power supplies and experiment control circuitry. The 30 cm long x 2 cm wide x 2.5 cm deep fuel tray was located inside a 10 cm x 10 cm cross-sectional area flow duct which provided a low-speed forced air flow over the fuel tray. Hot-wire igniters were located 1 cm from each end of the tray. Thermocouples were at several locations in the fuel and surrounding gas. The sides of the fuel tray were constructed of schlieren quality windows to allow viewing of the fuel from the side. The top and sides of the flow duct were also fitted with windows to allow recording of the propagating flame by eight camera systems. Two top cameras and two side cameras each recorded half of the flame spread. These images were video-mixed to generate two video signals, each with a top and side view. Two side-viewing PIV systems, with a wide Field Of View (FOV) — 2.5 cm x 10 cm — and a narrow FOV — 2 cm x 2.6 cm — respectively, recorded liquid-fuel flow patterns as the flame crossed the midsection of the tray. An infrared camera (8-12 μm spectral range) with

a 2.5 cm x 7 cm FOV through a salt window recorded the liquid surface temperature field ahead of the flame crossing this same region. Finally, an RSD system with a 10 cm circular FOV centered at the axial midpoint of the tray recorded liquid-phase temperature gradients.

The experiment payload was a sealed pressure vessel filled with dry air so the experiment could be conducted at 1 atm (actual pressure at ignition was 15.1 psia due to heating during ascent). The temperature of the air and fuel was 20.5 °C at the time of ignition. The experiment operated autonomously, except for selected data downlink and uplink capabilities so the operation of the experiment could be observed in real-time and the igniters and the air flow could be controlled. The sounding rocket flight provided just over 6 minutes of μg time to perform the experiment. Seventy-five seconds after launch, the rocket was in μg and the experiment payload was energized. The 1-butanol fuel circulated internally for 60 s before filling the tray to ensure the PIV particles were well distributed in the fuel. The fuel tray was then filled completely by turning a valve which routes the fuel to the tray. Filling the tray in μg required 75 s; only a very few small bubbles located near the bottom of the fuel tray were observed and they did not apparently affect subsequent observations. This was an important engineering accomplishment regarding fuel management in μg. The experiment depended on surface tension and a sharp "pinning" edge at the inside top of the tray edges to maintain the fuel in the tray in μg. After filling the tray, a 10 cm/s bulk opposed air velocity (U_{opp}) was started. This value of U_{opp} was selected to be less than that normally found in 1g experiments of this scale, but much greater than diffusional velocities associated with quiescent, μg experiments. A 29 s waiting period then began, which allowed any pool surface deformations to damp out and any internal fluid motion from the filling process to cease (confirmed by PIV and RSD data). The primary igniter was then energized. Via an up-link manual command, the igniter was shut off once a flame appeared. At the end of the test, all experiment systems were de-energized and a valve was opened to the vacuum of space to evacuate the payload for safe handling upon retrieval. The evacuated payload returned to Earth via parachute and was recovered without damage one hour after flight.

Figure 1 shows a comparison between 1g and μg flame shapes (tick marks at the bottom of all figures indicate a cm scale). Note the absence of soot and a buoyant plume in the μg flame. In general the intensity of the μg flame was much less than the 1g flame; until it reached the tray midpoint, the μg flame front monotonically decreased in intensity as it propagated. The flame stood off the surface more in μg than in 1g. The top camera view showed that the 1g flame front was much less curved than the μg flame front, due most likely to the slower rate of propagation (discussed next) and increased sidewall heat and momentum losses in μg.

Figure 2 shows the flame position versus time for both 1g and μg. Ignition and spread are completed in 6–7 s in 1g. As expected, the 1g flame exhibits rapid, pulsating spread alternating in 1–2 s intervals between the slow and fast propagation phases of the pulsating cycle; the "crawling" velocity was 1–2 cm/s and the "jump" velocity was 8 cm/s. Ignition and spread took more than twice as long in μg. The character of the spread was also distinctly different than in 1g. In the first half of the tray, the flame moved slowly, without pulsation, and reached a near-steady spread velocity of about 1.5 cm/s; this value is an order of magnitude less than that which occurs in the 1g uniform spread regime, and is more similar to the crawling velocity described above. Just before the halfway position, the flame jumped forward at about 6 cm/s. It then paused at about the 20 cm position, which coincides with a thermocouple rake. After this, it rapidly and erratically spread. Hypotheses (not yet verified) as to why the flame spread behavior changed include: air flow irregularities, thermocouple rake interferences, mass flow reductions in the air stream due to heat release from the flame or pressure buildup, and ignition transients.

Figure 3 shows comparative 10 cm FOV RSD images centered at the midpoint of the fuel tray. The 1g image shows a series of vortices, close to the pool surface, which formed during 2–3 pulsation cycles when the flame slowly propagated. The μg image shows only 1 very large vortex, associated with the near-steady spread, which extends much deeper into the fuel depth and shows a much longer preheat distance. This clearly indicates that, consistent with numerical predictions [7], buoyancy stratifies the warmer liquid near the surface in 1g, which affects the liquid surface temperature profile that governs the thermocapillary-driven liquid surface velocity. Without appreciable buoyancy, the warm liquid is carried into the fuel depth by the thermocapillary-driven motion of the liquid fuel. The transfer of this energy deeper into the bulk fluid means less is available for surface preheating and evaporation, which is one reason the flame spread is slower. The steepness of the thermal gradients is such that in both 1g and μg the RSD image is driven off-scale near the

fuel surface.

A review of the PIV video indicates slow particle motion begins shortly after the igniter is energized in both 1g and μg. The flow accelerates sharply as the flame and its accompanying vortex approach. Figure 4 shows comparative PIV images for a time when the flame is near the center of the field of view. A time-lapse reconstruction of about 0.23 s is shown to clarify the flow patterns and average velocities. The center of the vortex under the flame is 7.2 mm deep in μg, compared to 3.8 mm in 1g. A comparison of the RSD and PIV images, as we noted in [4], shows how misleading refractive index measurement methods can be when used to infer flow pattern; for example the RSD shows nothing below the vortex, but the PIV clearly indicates motion near the bottom of the pool. We are presently in the process of measuring the detailed velocity field from the PIV.

Figure 5 shows comparative infrared images of the fuel surface temperature. Measurements of the absorption spectra as a function of liquid depth showed that 1-propanol and 1-butanol both are strong absorbers in the 8–12 μm range, thus the images are believed to represent surface or very near-surface temperatures. The camera was set for a 20–70 °C range, so when the flame entered the IR camera's field of view, it saturated the IR image; reconstruction of the visible flame position was possible, however, via the time-synchronization of all the video images. The 1g flame shows a unique structure we have called twinning. As the 1g flame began the crawling portion of the pulsating cycle, the preheat region extended, as expected, a greater distance ahead of the flame. It then developed very symmetric vortices which rolled up toward the side walls while a central portion of preheated liquid continued to proceed upstream of the flame. At a later time, the flame jumped forward and obscured the twin vortices. The cycle then repeated itself with the reformation of the twin vortices. The liquid preceding the μg flames showed an entirely different heating pattern; recall, in this case, the flame was spreading steadily and much more slowly. As also seen by the RSD, the IR revealed the preheat distance ahead of the flame was much greater in μg than in 1g. While the flame itself showed side-to-side symmetry, no twin structures were observed in the IR image. Instead, asymmetric vortical motion was clearly apparent in μg. To summarize, the IR images show several novel findings. First, the IR view implied significant sideflow in both 1g and μg. This has not been revealed by line-of-sight, refractive index methods to date or by the shape of the visible flame front. Furthermore, these 3D spanwise effects cannot be predicted by current 2D numerical models. Secondly, symmetrical processes were found in 1g but not in μg. Third, a much longer preheat region exists in μg. Finally, Fig. 5 shows that a surface temperature valley exists ahead of portions of the flame leading edge, caused by fingers of hot liquid that curl sideways trapping cooler liquid between them and the flame front. This result is consistent with the observation reported in [8] and heretofore unverified or unexplained.

Numerical Modeling

Figure 6 shows the geometry and select boundary condition and grid construction information for the numerical model used to simulate the sounding rocket experiment. The gravity level is assumed to be zero in the simulations reported herein. Using a gravity of 10^{-4} g yields essentially identical results. The igniter (size = 0.4 x 0.09 mm) is modeled as a hot pocket of gas with a temperature that increases linearly from $T_o = 21$ ° C to 1700 K in 0.2 s. The igniter temperature remains constant until the flame reaches the location $x_{\mathrm{fl}} = 3$ cm, after which time the temperature of the igniter is no longer held fixed (i.e., the hot pocket of gas is treated the same as any other point in the interior of the domain). The initial condition for the streamwise velocity, $u(x, y)$, is equal to the inlet boundary condition at $x = 32$ cm. A linear inlet velocity profile is used for $0 < y < 0.5$ mm to avoid unrealistically high initial shear stresses at the liquid surface. For $y \geq 0.5$ mm, the inlet velocity is uniform and equal to 10 cm/s. The other boundary conditions at the inlet of the gas phase are $h_1 = h_{1,o}$, $v = 0$, $Y_F = Y_P = 0$, and $\chi_{O_2} = 0.21$. The boundary conditions at the outlet of the gas phase ($x = 0$) are given in Figure 6. A convective boundary condition for u yields slightly better convergence and satisfaction of global continuity as compared to a zero normal gradient condition, $\partial u/\partial x = 0$. The initial condition for the fuel vapor concentration in the gas phase is assumed to be $\chi_{F,o} = P_{\mathrm{sat}}(T_o) \exp[-y/(1\ \mathrm{mm})]$. Prior to activating the igniter, the fuel is allowed to vaporize and convect/diffuse through the gas phase in the presence of the forced opposed flow without external heating for 6 s. This results in a steady fuel vapor concentration profile at the time of ignition.

The boundary conditions at the gas/liquid interface include balance of the stresses, continuity of the tangential velocity, no dissolving of air into the liquid (Stefan flow assumption), neglect of recession of the

liquid surface, balance of the normal heat flux, and continuity of the temperature. A nonuniform grid is used in the x and y directions in both phases. Since the thickness of the reaction zone in the flame leading edge region is two orders of magnitude smaller than the length of the computational domain, a partially adaptive gridding scheme is used in the x-direction to provide fine resolution of the steep gradients in the reaction zone throughout the simulation. As shown in Figure 6, a uniform mesh of $\Delta x_{\text{fl}} = 0.4$ mm is used in a 4 mm region around the flame. Behind and ahead of this region, the mesh size increases with geometric progression factors. A 132 x 102 gas-phase mesh, 132 x 52 liquid-phase mesh, and 1 ms time step were used for the calculations. Each simulation exhibited excellent convergence and satisfaction of global continuity. Other details of the numerical model and the governing equations are the same as for the open pool configuration without forced flow described in [5].

Figure 2 summarizes the numerical results for $U_{\text{opp}} = 10$ cm/s and different values of the input parameters A (nondimensional pre-exponential constant) and E_a (nondimensional activation energy). These parameters are nondimensionalized using reference values of $E_{a,*} = 30$ kcal/gmole and $A_* = 4.69 \times 10^{11}$ m^3/(kmol·s) (taken from [9] and previous calculation for propanol [5]). As shown in Figure 2, the numerical results are sensitive to the choice of activation energy, E_a, and (to a lesser extent) pre-exponential constant, A, for the first-order, finite chemical reaction rate expression. For unity values of A and E_a, the flame remained at the igniter location, $x = 1$ cm, when the simulation was halted 15 s after the igniter was activated. The flame extinguishes quickly if the igniter is subsequently de-activated.

In all the cases except for $A = 1$ and $E_a = 0.8$ (which yielded uniform flame spread with very little ignition transient), after the igniter is activated the flame initially spreads very slowly (with speed 0.5–2 cm/s) and a relatively large region of liquid flow forms ahead of the flame. The overall length of this flow ahead of the flame, δ_{flow}, is due to the ignition transient and is appreciably larger than that which is formed during the subsequent flame spread. After this initial period during which the flame spreads slowly, the flame accelerates across a distance of order δ_{flow} at approximately 20 cm/s. The ensuing flame spread consists of a series of slow-moving and rapid-moving movements across the liquid surface. In some cases, the flame moves backward before accelerating forward. The pulsation frequency increases with increasing A or decreasing E_a. A comparison of runs with $E_a = 1$ and $A = 3$, 5 and 8 indicate that the mean flame spread rate, $\overline{U}_{\text{fl}}$, after the ignition transient does not vary strongly with A. The dependence appears to be much weaker than $\overline{U}_{\text{fl}} \propto \sqrt{A}$, which one would expect if most of the flame advancement was of a premixed nature.

Simulations were performed for a range of U_{opp} from 1 cm/s to 30 cm/s for $A = 5$ and $E_a = 1$. For $U_{\text{opp}} \geq 10$ cm/s, as U_{opp} increases, the flame begins to propagate sooner (i.e., the ignition transient decreases), the pulsation frequency increases, and the mean flame speed increases slightly. Consistent with results of μg experiments conducted in the NASA-LeRC Zero Gravity Facility, the flame extinguishes in a nearly quiescent environment ($U_{\text{opp}} = 1$ cm/s). For $U_{\text{opp}} = 10$ cm/s, flame pulsations occur more frequently and regularly for a 5 mm pool depth compared to a 25 mm depth. This suggests that one can reduce the ignition transient and increase the number of pulsations in μg experiments by using a shallower pool.

The conditions which yield pulsating flame spread in normal gravity without forced opposed flow appear to be the same as those which cause pulsating flame spread at zero gravity or microgravity with forced opposed flow. The flame spread mechanism was described in detail in [5] and is briefly summarized here. Figure 7 shows details of the zero gravity flow field, contours of Y_F, Y_{O_2} and fuel consumption rate, and liquid surface temperature and velocity data near the flame leading edge at the beginning of a pulsation cycle for $A = 5$, $E_a = 1$. This figure shows that the liquid surface is heated up to 2 cm ahead of the flame leading edge. The liquid surface velocity in this region is due to thermocapillary convection. Pulsating flame spread is caused by a gas-phase recirculation cell which entrains fuel vapor just ahead of the flame leading edge. This recirculation cell forms due to the combination of thermocapillary-driven concurrent flow of the liquid surface and opposed gas-phase flow (due to the forced inlet flow in this case, or due to buoyancy in 1g). While the recirculation cell entrains fuel vapor, the maximum fuel consumption rate is relatively small and the flame propagates slowly at a speed of 1–2 cm/s. When the fuel vapor concentration ahead of the flame approaches a lean flammability limit, the maximum reaction rate increases significantly, causing the flame to accelerate up to a speed of the same order as the lean-limit, premixed laminar flame speed. Simultaneously, the increased rate of hot gas expansion destroys the recirculation cell structure ahead of the flame by forcing the flow to diverge away from the flame leading edge rather than be drawn toward the liquid surface by shear induced from the liquid motion. After the flame accelerates through the premixed region that was formed in

the recirculation cell, the maximum reaction rate and the rate of hot gas expansion decrease, thus allowing the forced flow to create opposed flow just ahead of the flame leading edge. The reduction in the hot gas expansion also allows the gas-phase shear from the liquid surface motion to pull the gas just ahead of the flame toward the liquid surface and thus re-form the recirculation cell.

Future Work

Two additional sounding rocket experiments are presently scheduled to take place within the next year. The gas-phase thermocouple and some of the subsurface thermocouple rake which apparently restrained flame propagation in μg will be removed or re-positioned to produce less obstruction. Test conditions for the flights are being established, and will likely be at different opposed flow velocities, spanning values closer to those found naturally in 1g buoyant situations and then to those closer to near-quiescent conditions. Supporting ground-based tests in drop tower facilities will be utilized to establish that a flame will be sustained in these conditions at least for the first few seconds of μg (the sounding rocket experiments are needed to verify their persistence). Tests in 1g with various tray widths may commence. Additional μg tests (in a sounding rocket) with a concurrent air flow will be sought to complete the originally proposed test matrix. Modeling will continue for the 1g open pool and forced flow cases in which numerical convergence is challenging due to buoyancy-induced vorticity which must be convected past an artificially imposed outflow boundary. In addition, we will continue numerical calculations to predict μg flame spread behavior in both the opposed flow and concurrent flow cases.

Acknowledgments: The computational research was supported in part by the San Diego Supercomputer Center and NASA Center for Computational Sciences through allocations of computer time. The Lewis and Case Western researchers wish to acknowledge the build-up and test support provided by the Spread Across Liquids (SAL) engineering team at Lewis, and the rocket launch expertise provided by Wallops Island Flight Facility and White Sands Missile Range personnel.

References

1. Ross, H. D., " Ignition of and Flame Spread Over Laboratory-Scale Pools of Pure Liquid Fuels," *Prog. Energy Combust. Sci.*, Vol. 20, 1994, pp. 17–63.

2. Sirignano, W. A. and Schiller, D. N., "Mechanisms of Flame Spread Across Condensed-Phase Fuels," to appear in *Comb. Sci. Tech.* Book Series honoring Professor Irvin Glassman, 1995.

3. Miller, F. J., Ross, H. D., and Schiller, D. N., "Temperature Field During Flame Spread over Alcohol Pools: Measurements and Modelling," presented at the Eastern States Section, Combustion Institute, Clearwater, FL, 1994.

4. Miller, F. J. and Ross, H. D., "Liquid-Phase Velocity and Temperature Fields During Uniform Flame Spread over 1-Propanol," accepted for Eighth Int'l Symp. on Transport Processes, San Francisco, CA, July, 1995.

5. Schiller, D. N., Ross, H. D., and Sirignano, W. A., "Computational Predictions of Flame Spread over Alcohol Pools," AIAA-93-0825, 31st AIAA Aero. Sci. Mtg., Reno, Nevada, 1993; submitted to *Comb. Sci. Tech.* as "Computational Analysis of Flame Spread over Alcohol Pools."

6. Ito, A., Masuda, D., and Saito, K., "A Study of Flame Spread Over Alcohols Using Holographic Interferometry," *Combustion and Flame*, Vol. 83, 1991, pp. 375–389.

7. Schiller, D. N. and Sirignano, W. A., "Buoyant-Thermocapillary Flow With Nonuniform Supra-Heating: I. Liquid-Phase Behavior," *Journal of Thermophysics and Heat Transfer*, Vol. 6, No. 1, Jan. 1992, pp. 105–112.

8. Glassman, I. and Dryer, F., "Flame Spread Across Liquid Fuels," *Fire Safety J.*, Vol. 3, 1980/1981, pp. 123–138.

9. Westbrook, C. K. and Dryer, F. L., "Simplified Reaction Mechanisms for the Oxidation of Hydrocarbon Fuels in Flames," *Comb. Sci. Tech.*, Vol. 27, 1981, pp. 31–43.

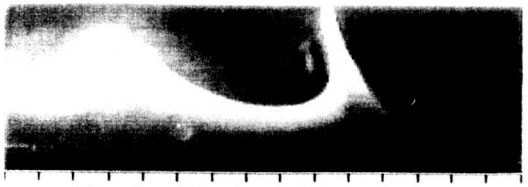

Fig. 1a Side view of flame in 1-g.

Fig. 1b Side view of flame in 0-g

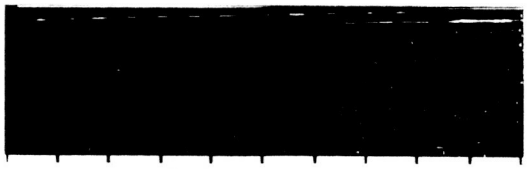

Fig. 4a Particle Tracks for 1-g spread

Fig. 4b Particle Tracks for 0-g spread

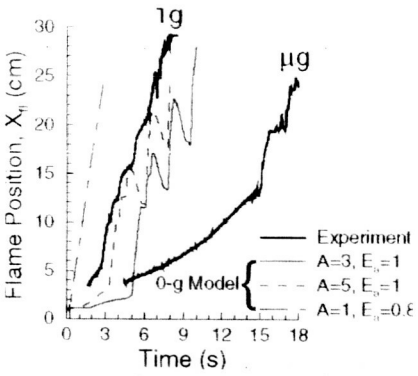

Fig. 2 Flame position vs. time

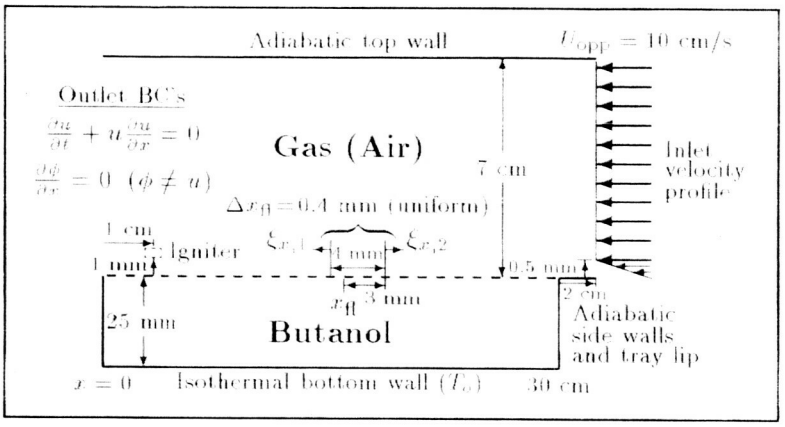

Fig. 6. Schematic of computational domain and boundary conditions for model

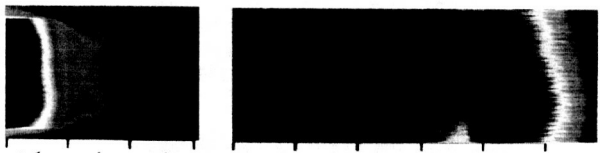

a) 1-g prior to jump b) 1-g after jump (0.5 s later)

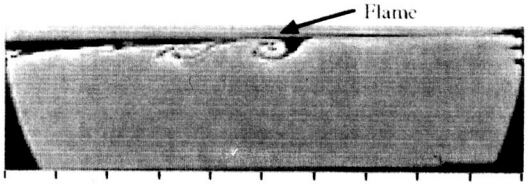

Fig. 3a Schlieren view of liquid in 1-g.

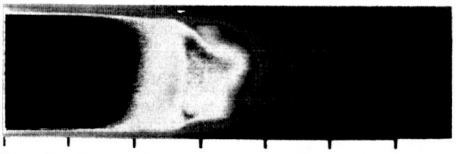

Fig. 5. Pool surface temperature. c) 0-g

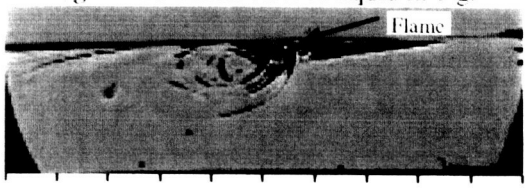

Fig. 3b Schlieren view of liquid in 0-g

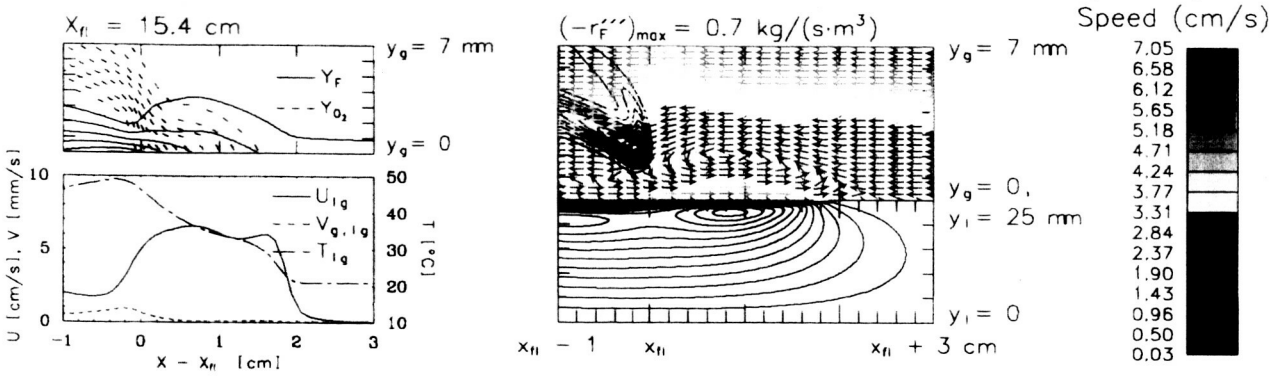

Fig. 7 Predicted velocity, fuel concentration, temperature, and flow field contours (A = 5, E_a = 1, t = 5.0 s)